Earth and Planetary Science Letters 511 (2019) 44–54

Contents lists available at ScienceDirect

Earth and Planetary Science Letters

www.elsevier.com/locate/epsl

# Origin of the non-carbonaceous–carbonaceous meteorite dichotomy

Josefine A.M. Nanne [a], Francis Nimmo [b], Jeffrey N. Cuzzi [c], Thorsten Kleine [a,*]

[a] Institut für Planetologie, University of Münster, Wilhelm-Klemm-Straße 10, 48149 Münster, Germany
[b] Department of Earth and Planetary Sciences, University of California Santa Cruz, Santa Cruz, CA 95064, USA
[c] Space Science Division, Ames Research Center, Moffett Field, CA 94035, USA

ARTICLE INFO

*Article history:*
Received 29 November 2018
Received in revised form 15 January 2019
Accepted 17 January 2019
Available online 1 February 2019
Editor: F. Moynier

*Keywords:*
nickel isotopes
meteorite dichotomy
iron meteorites
infall
nucleosynthetic anomalies

ABSTRACT

The isotopic composition of meteorites reveals a fundamental dichotomy between non-carbonaceous (NC) and carbonaceous (CC) meteorites. However, the origin of this dichotomy—whether it results from processes within the solar protoplanetary disk or is an inherited heterogeneity from the solar system's parental molecular cloud—is not known. To evaluate the origin of the NC–CC dichotomy, we report Ni isotopic data for a comprehensive set of iron meteorites, with a special focus on groups that have not been analyzed before and belong to the CC group. The new Ni isotopic data demonstrate that the NC–CC dichotomy extends to Ni isotopes, and that CC meteorites are characterized by a ubiquitous $^{58}$Ni excess over NC meteorites. These data combined with prior observations reveal that, in general, the CC reservoir is characterized by an excess in nuclides produced in neutron-rich stellar environments, such as $^{50}$Ti, $^{54}$Cr, $^{58}$Ni, and *r*-process Mo isotopes. Because the NC–CC dichotomy exists for refractory (Ti, Mo) and non-refractory (Ni, Cr) elements, and is only evident for nuclides produced in specific, neutron-rich stellar environments, it neither reflects thermal processing of presolar carriers in the disk, nor the heterogeneous distribution of isotopically anomalous Ca–Al-rich inclusions (CAI). Instead, the NC–CC dichotomy reflects the distinct isotopic composition of later infalling material from the solar system's parental molecular cloud, which affected the inner and outer regions of the disk differently. Simple models of the infall process by themselves can support either infall of increasingly NC-like material onto an initially CC-like disk, or infall of increasingly CC-like material in the absence of disk evolution by spreading. However, provided that CAIs formed close to the Sun, followed by rapid outward transport, their isotopic composition likely reflects that of the earliest infalling material, implying that the composition of the inner disk (i.e., the NC reservoir) is dominated by later infalling material, whereas the outer disk (i.e., the CC reservoir) preserved a compositional signature of the earliest disk. The isotopic difference between the inner and outer disk was likely maintained through the rapid formation of Jupiter, which prevented complete homogenization between material from inside (NC reservoir) and outside (CC reservoir) its orbit.



## 1. Introduction

The isotopic composition of meteorites reveals a fundamental dichotomy in their genetic heritage, distinguishing between non-carbonaceous (NC) and carbonaceous (CC) meteorites. This dichotomy was first recognized by Warren (2011), who observed that the Cr, Ti, and O isotopic compositions of meteorites define two distinct clusters. Subsequent work has shown that this dichotomy extends to Mo isotopes and includes both chondrites and differentiated meteorites, including iron meteorites (Budde et al., 2016; Kruijer et al., 2017). The latter derive from bodies that accreted within ~1 Ma after formation of Ca,Al-rich inclusions (CAI) (Kruijer et al., 2014), implying that the distinct isotopic compositions of the NC and CC reservoirs had been established by this time (Kruijer et al., 2017). As chondrites, which derive from parent bodies that accreted up to ~3–4 Ma later than the iron meteorite parent bodies (e.g., Budde et al., 2018; Kita and Ushikubo, 2012; Kleine et al., 2018; Krot et al., 2009; Nagashima et al., 2017; Ushikubo et al., 2013; Villeneuve et al., 2009), display the same fundamental dichotomy as the iron meteorites, the NC and CC reservoirs must have coexisted in the early solar nebula for at least ~3–4 Ma without any significant exchange of material between the two reservoirs. This prolonged spatial separation of the NC and CC reservoirs is most likely attributable to the early formation and growth of Jupiter's core, which prevented material exchange between inside (NC) and outside (CC) its orbit (Budde et al., 2018;

* Corresponding author.
*E-mail address:* thorsten.kleine@wwu.de (T. Kleine).

https://doi.org/10.1016/j.epsl.2019.01.027

Kruijer et al., 2017). However, the origin of the NC–CC dichotomy and the processes that led to the establishment of two isotopically distinct reservoirs are not understood.

With the exception of O, the isotopic dichotomy between NC and CC meteorites is nucleosynthetic in origin, reflecting the heterogeneous distribution of isotopically diverse presolar components. The NC–CC dichotomy is most clearly seen in the isotopic compositions of Ti, Cr, and Mo, where the CC reservoir is characterized by enrichments in the neutron-rich isotopes $^{50}$Ti, $^{54}$Cr, and in Mo isotopes produced in the rapid neutron capture process (*r*-process) of stellar nucleosynthesis (Budde et al., 2016; Kruijer et al., 2017; Poole et al., 2017; Warren, 2011; Worsham et al., 2017). There are two general categories of processes by which the distinct isotopic composition of the NC and CC reservoirs may have been generated. One possibility is that this reflects thermal processing, transport, and mixing of presolar carriers within the solar protoplanetary disk (Burkhardt et al., 2012; Trinquier et al., 2009). Intriguingly, the isotope characteristics of the CC reservoir resemble those found in CAIs, and so it has been suggested that the NC–CC dichotomy reflects a larger proportion of CAI-like material in the CC compared to the NC reservoir (Budde et al., 2016; Gerber et al., 2017). Another possibility is that the NC–CC dichotomy does not result from processes within the disk itself, but reflects heterogeneities in the solar system's parental molecular cloud. The distance where mass is added to the disk from the collapsing protostellar envelope grows with time (Hueso and Guillot, 2005), and so different areas of the disk received different proportions of material infalling at different times. Thus, changes in the isotopic composition of the infalling material may have generated heterogeneities in the disk as a function of heliocentric distance (Dauphas and Schauble, 2016).

Nickel isotopes are well suited to distinguish between these possibilities and, hence, to constrain the processes by which the distinct isotopic compositions of the NC and CC reservoirs were established. Nickel belongs to the Fe-peak elements and contains five stable isotopes ($^{58}$Ni, $^{60}$Ni, $^{61}$Ni, $^{62}$Ni, and $^{64}$Ni) that are dominantly produced during nuclear statistical equilibrium (the *e*-process) in both type Ia and type II supernovae (Burbidge et al., 1957). Nickel is a moderately siderophile element and a major component in both stony and iron meteorites, meaning that, unlike for elements like Cr and Ti, it can be analyzed in essentially all meteorite groups. Perhaps most importantly with regard to the NC–CC dichotomy, Ni is non-refractory and therefore not enriched in CAIs. Thus, if the NC–CC dichotomy exists for Ni, then this dichotomy cannot be the result of a minor amount of CAI addition to the CC reservoir.

Prior studies have shown that bulk meteorites exhibit nucleosynthetic Ni isotope anomalies, and that these anomalies seem to be distinct for NC and CC meteorites (Regelous et al., 2008; Steele et al., 2012, 2011; Tang and Dauphas, 2014, 2012). Specifically, group IVB iron meteorites seem to be genetically linked to carbonaceous chondrites, whereas some other groups (IC, IIAB, IIIAB, IVA) are more similar to ordinary and enstatite chondrites (Regelous et al., 2008). However, with the exception of the IVB irons, no Ni isotope data for iron meteorites belonging to the CC suite (i.e., groups IIC, IID, IIF, and IIIF) have been reported, yet these irons are essential for assessing whether the NC–CC dichotomy holds for Ni isotopes, because they record the onset time at which the NC–CC dichotomy was established.

Here, Ni isotopic data for several iron meteorite groups are presented, with emphasis on CC iron meteorite groups for which no Ni isotopic data have been previously reported. The new data are used to assess whether the NC–CC dichotomy holds for Ni isotopes, and, ultimately, to identify the processes by which the distinct isotopic compositions of the NC and CC reservoirs were established.

## 2. Samples and analytical methods

### 2.1. Sample selection and preparation

For this study, 19 different iron meteorites from the chemical groups IC, IIC, IID, IIIE, IIF, IIIF, and IVA were selected. Except for the IC and IVA irons, no samples from these groups have previously been investigated for Ni isotope systematics. Moreover, the selected samples include both carbonaceous (IIC, IID, IIF, IIIF) as well as non-carbonaceous irons (IC, IIIE, IVA), as determined based on their Mo isotope systematics. In addition to the iron meteorites, the NIST steel SRM361, USGS Hawaiian basalt BHVO-2 and the CV3 chondrite Allende ('MS-A', prepared from a bulk piece of ~100 g) were analyzed. Nickel isotopic data for these three samples were reported in previous studies, facilitating comparison of the results between this and previous studies.

All iron meteorite samples (~0.3–0.6 g) were cut using a diamond saw, polished with abrasives (SiC) and ultrasonically cleaned in ethanol. Further, to remove any surficial contamination, samples were leached in 6 M HCl for 10 minutes at ~70 °C. Afterwards, they were digested in 6 M HCl with traces of $HNO_3$ in Teflon beakers placed on a hot plate at 130 °C for 24–48 h. Small aliquots of these digestion solutions (corresponding to ~20–25 µg of Ni) were further processed for the Ni isotope measurements. The SRM361 steel was digested and aliquoted in the same way as the iron meteorites.

BHVO-2 and Allende were digested in a 2:1 mixture of $HNO_3$ and HF in Teflon beakers for 48 h at 180 °C. After digestion, the samples were evaporated to dryness and re-dissolved in $HNO_3$. This step was repeated three times. Subsequently, the samples were re-dissolved in reverse *aqua regia* and fluxed for 72 h at 150 °C. Finally, the samples were taken up in 6 M HCl for column chemistry. In addition, an aliquot of the Ni standard solution NIST SRM 986 was dried down, re-dissolved in 6 M HCl, and processed alongside the samples.

### 2.2. Chemical separation

Chemical purification of Ni was achieved by a 3-step ion exchange chromatographic procedure following the method of Chernonozhkin et al. (2015). Samples were first loaded in 10 ml 0.6 M HCl–90% acetone onto BioRad polyprep columns filled with 2 ml pre-cleaned and conditioned BioRad AG 50WX4 cation exchange resin (200-400 mesh). Most of the sample matrix (e.g., Fe, Cr) was eluted with additional 35 ml 0.6 M HCl–90% acetone and 10 ml 0.6 M HCl–95% acetone, before Ni was collected in 6 ml 0.6 M HCl–95% acetone–0.1 M dimethylglyoxime (DMG). After drying down the Ni fractions with the addition of 14 M $HNO_3$, the samples were fluxed twice in 0.3 ml 14 M $HNO_3$–0.1 ml 30% $H_2O_2$ for 2–3 h at 140 °C, and in 0.4 ml *aqua regia* for 3 h at 140 °C. This procedure resulted in efficient destruction of organic material from the cation resin. The main purpose of the second chemistry is the removal of any Zn and Ti from the sample solutions. For this chemistry, the Ni fractions were evaporated to dryness and re-dissolved several times in 10 M HCl, and finally taken up in 2 ml 0.5 M HF–1 M HCl. This solution was loaded onto BioRad polyprep columns filled with 2 ml pre-cleaned and conditioned BioRad AG1X8 anion exchange resin (100–200 mesh). On this column, Ni was eluted with addition of 7 ml 0.5 M HF–1 M HCl. The Ni cut was dried down and re-dissolved several times with 10 M HCl. Finally, to remove residual Zn and Fe, the Ni cuts from the second chemistry were re-dissolved in 1 ml 6 M HCl–0.01% $H_2O_2$ and loaded onto BioRad polyprep columns filled with 2 ml of pre-cleaned and conditioned AG MP-1X4 anion exchange resin (100–200 mesh). Again, Ni was eluted with addition of 5 ml 6 M HCl–0.01% $H_2O_2$. The final Ni solution was evaporated to dryness

**Table 1**
Ni isotopic data.

| Sample | Class | $\varepsilon^{196}$Pt | $N$ | Norm. $^{61}$Ni/$^{58}$Ni | | | Norm. $^{62}$Ni/$^{61}$Ni | | |
|---|---|---|---|---|---|---|---|---|---|
| | | | | $\mu^{60}$Ni ($\pm2\sigma$) | $\mu^{62}$Ni ($\pm2\sigma$) | $\mu^{64}$Ni ($\pm2\sigma$) | $\mu^{58}$Ni ($\pm2\sigma$) | $\mu^{60}$Ni ($\pm2\sigma$) | $\mu^{64}$Ni ($\pm2\sigma$) |
| Terrestrial samples | | | | | | | | | |
| NIST SRM 986 | | n.d. | 20 | −1 ± 2 | 1 ± 4 | −2 ± 8 | 3 ± 11 | 0 ± 4 | −5 ± 12 |
| NIST SRM 361 #1 | | n.d. | 17 | 0 ± 3 | 4 ± 6 | −3 ± 12 | 12 ± 16 | 4 ± 6 | −15 ± 18 |
| NIST SRM 361 #2 | | n.d. | 10 | −2 ± 2 | 1 ± 6 | 3 ± 7 | 3 ± 16 | −1 ± 6 | 0 ± 17 |
| BHVO-2 | | n.d. | 15 | 0 ± 3 | 3 ± 9 | 3 ± 16 | 9 ± 24 | 3 ± 9 | −6 ± 27 |
| Carbonaceous chondrites | | | | | | | | | |
| Allende | CV3 | n.d. | 16 | −11 ± 3 | 12 ± 6 | 29 ± 13 | 37 ± 16 | 1 ± 6 | −6 ± 19 |
| Carbonaceous iron meteorites | | | | | | | | | |
| Kumerina | IIC | 0.02 | 21 | −18 ± 3 | 9 ± 6 | 21 ± 13 | 28 ± 16 | −9 ± 6 | −6 ± 19 |
| Perryville #1 | IIC | 0.05 | 16 | −16 ± 5 | 20 ± 9 | 52 ± 29 | 62 ± 24 | 4 ± 9 | −7 ± 33 |
| Perryville #2 | IIC | 0.05 | 16 | −16 ± 3 | 20 ± 5 | 55 ± 12 | 62 ± 14 | 4 ± 5 | −4 ± 16 |
| Unter−Mässing | IIC | 0.12 | 15 | −14 ± 3 | 16 ± 5 | 33 ± 11 | 50 ± 14 | 2 ± 5 | −14 ± 16 |
| Wiley | IIC | 0.06 | 16 | −17 ± 3 | 13 ± 5 | 34 ± 10 | 40 ± 14 | −4 ± 5 | −4 ± 15 |
| Bridgewater #1 | IID | −0.01 | 15 | −12 ± 3 | 22 ± 6 | 41 ± 12 | 68 ± 16 | 10 ± 14 | −24 ± 13 |
| Bridgewater #2 | IID | −0.01 | 15 | −10 ± 2 | 16 ± 3 | 31 ± 12 | 50 ± 8 | 6 ± 7 | −16 ± 12 |
| N'Kandhla | IID | 0.01 | 16 | −9 ± 3 | 18 ± 6 | 38 ± 9 | 56 ± 16 | 9 ± 14 | −15 ± 10 |
| Del Rio | IIF | 0.04 | 13 | −9 ± 1 | 9 ± 4 | 17 ± 11 | 28 ± 11 | 0 ± 9 | −10 ± 11 |
| Clark County #1 | IIIF | 0.06 | 20 | −14 ± 3 | 17 ± 7 | 36 ± 14 | 53 ± 19 | 3 ± 16 | −14 ± 15 |
| Clark County #2 | IIIF | 0.06 | 13 | −10 ± 3 | 11 ± 5 | 26 ± 16 | 34 ± 14 | 1 ± 12 | −7 ± 16 |
| Oakley | IIIF | 0.48 | 16 | −9 ± 4 | 9 ± 7 | 18 ± 10 | 28 ± 19 | 0 ± 16 | −9 ± 12 |
| Non-carbonaceous iron meteorites | | | | | | | | | |
| Arispe | IC | 0.33 | 16 | −8 ± 3 | −7 ± 5 | −29 ± 9 | −22 ± 14 | −15 ± 12 | −8 ± 10 |
| Bendego | IC | 0.50 | 14 | −7 ± 2 | −10 ± 7 | −37 ± 15 | −31 ± 19 | −17 ± 16 | −7 ± 16 |
| Chihuahua City | IC | 0.07 | 16 | −5 ± 2 | −2 ± 7 | −16 ± 18 | −6 ± 19 | −7 ± 16 | −10 ± 18 |
| Mount Dooling | IC | 0.00 | 13 | −4 ± 4 | −2 ± 5 | −10 ± 12 | −6 ± 14 | −6 ± 12 | −4 ± 12 |
| Murnpeowie | IC | 0.32 | 15 | −5 ± 3 | −4 ± 6 | −17 ± 12 | −12 ± 16 | −9 ± 14 | −5 ± 13 |
| Burlington | IIIE | 0.07 | 16 | −6 ± 2 | −4 ± 4 | −14 ± 10 | −12 ± 11 | −10 ± 9 | −2 ± 10 |
| Coopertown | IIIE | 0.02 | 14 | −8 ± 2 | −8 ± 5 | −25 ± 13 | −25 ± 14 | −16 ± 11 | −1 ± 13 |
| Paneth's iron | IIIE | 0.09 | 16 | −5 ± 3 | −9 ± 5 | −33 ± 12 | −28 ± 14 | −14 ± 12 | −6 ± 12 |
| Willow Creek #1 | IIIE | 0.13 | 15 | −9 ± 4 | −4 ± 8 | −20 ± 18 | −12 ± 22 | −13 ± 18 | −8 ± 19 |
| Willow Creek #2 | IIIE | 0.13 | 16 | −4 ± 3 | −10 ± 5 | −38 ± 12 | −31 ± 14 | −14 ± 12 | −8 ± 12 |
| Gibeon #1 | IVA | 0.13 | 15 | −9 ± 4 | −14 ± 6 | −32 ± 18 | −43 ± 16 | −23 ± 14 | 9 ± 18 |
| Gibeon #2 | IVA | 0.13 | 15 | −6 ± 3 | −1 ± 5 | −15 ± 13 | −3 ± 14 | −7 ± 12 | −12 ± 13 |

$\mu^{i}Ni = ([^{i}Ni/^{58}Ni]_{sample}/[^{i}Ni/^{58}Ni]_{SRM986} - 1) \times 10^{6}$ for the $^{61}$Ni/$^{58}$Ni normalization.
$\mu^{i}Ni = ([^{i}Ni/^{61}Ni]_{sample}/[^{i}Ni/^{61}Ni]_{SRM986} - 1) \times 10^{6}$ for the $^{62}$Ni/$^{61}$Ni normalization.
Uncertainties are 95% confidence intervals.
$\varepsilon^{196}$Pt values from Kruijer et al. (2017) and Matthes et al. (2018).
$N$ = number of measurements.

and re-dissolved several times in $HNO_3$, before taking the solution up in 0.3 M $HNO_3$ for analysis by MC-ICP-MS. The final $^{58}$Fe/$^{58}$Ni and $^{64}$Zn/$^{64}$Ni ratios of the purified Ni cuts of all samples were $<9 \times 10^{-6}$ and $<9 \times 10^{-4}$, respectively, and sufficiently low for accurate correction of isobaric interferences (Render et al., 2018).

This 3-step column procedure was tested and calibrated by processing the Ni standard solution SRM 986, the steel standard SRM 361, the iron meteorite Gibeon, and BHVO-2. For all samples, consistent elution profiles were obtained and the final Ni cuts were sufficiently clean for isotopic analyses. The total yield of the entire procedure for processed samples was ∼90%. Total procedure blanks were <15 ng Ni and, hence, negligible given the amount of Ni analyzed for each sample.

### 2.3. Isotope measurements

Nickel isotope measurements were performed on the Thermo Scientific Neptune *Plus* MC-ICP-MS at the Institut für Planetologie. The purified Ni fractions were dissolved in 0.3 M $HNO_3$ and introduced into the mass spectrometer using a Savillex C-Flow PFA nebulizer connected to a Cetac Aridus II desolvator at an uptake rate of ∼50 µL/min. A combination of standard sampler and X-skimmer cones were used, and measurements were made at medium mass resolution on the left shoulder of the peak plateau to avoid possible interferences on mass 57 from $^{40}Ar^{16}OH$ or $^{40}Ar^{17}O$ (Tang and Dauphas, 2012). Using this set-up, the instrument sensitivity for $^{58}$Ni was ∼110 V/ppm. Samples and standards were typically measured with ∼95 V on mass 58, as intensities were limited due to the use of a $10^{11}$ Ω resistor on mass 60 (for which signals were <40 V). Ion beams at masses 58, 60, 61, 62 and 64 were simultaneously collected in a single cycle. In addition to the Ni masses, ion beams at masses 57 and 66 were also monitored to correct for potential isobaric interferences from $^{58}$Fe and $^{64}$Zn. All ion beams were collected in Faraday cups connected to amplifiers with $10^{11}$ Ω feedback resistors, except for $^{58}$Ni ($10^{10}$ Ω resistor) as well as $^{57}$Fe and $^{66}$Zn ($10^{12}$ Ω resistors). Prior to each sample or standard measurements, baselines were measured as on peak zeros (OPZ) for 30 × 8.4 s using the same acid solution used for the sample and standard dilutions. Each sample or standard measurement consisted of 50 cycles of 8.4 s integrations each, and each sample solution was analyzed 10–21 times, bracketed by analyses of the Ni solution standard SRM 986. The Ni concentrations of the sample solutions were matched to within 5% of the SRM 986 solution.

All samples and standards are mass bias-corrected by internal normalization to either $^{61}$Ni/$^{58}$Ni = 0.016744 or $^{62}$Ni/$^{61}$Ni = 3.1884 (Gramlich et al., 1989) using the exponential law. The data are reported as $\mu$ values, which are the parts-per-million deviation relative to the mean Ni isotopic composition measured for NIST SRM 986 before and after each sample (Table 1). Uncertainties are reported as 95% confidence limits of the mean of pooled solution replicates.

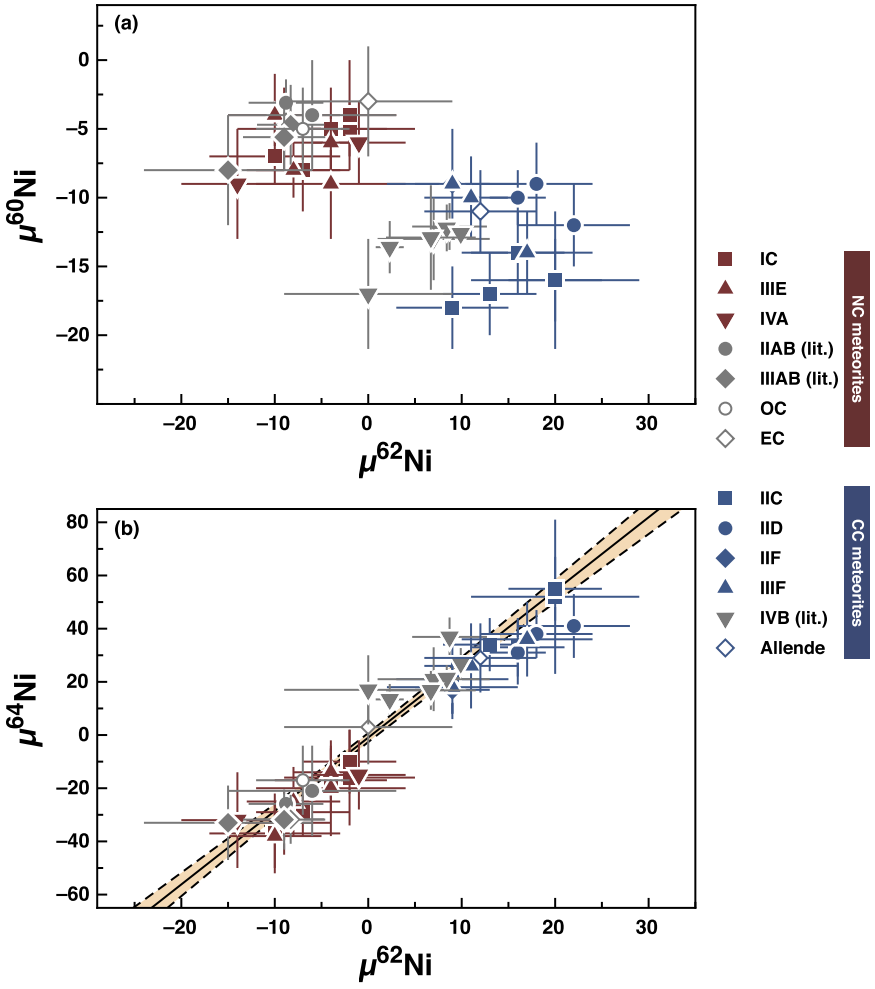


**Fig. 1.** Nickel isotope compositions, normalized to $^{61}$Ni/$^{58}$Ni, for iron meteorites (filled symbols) and chondrites (open symbols). Data from this study are shown in red (NC meteorites) and blue (CC meteorites). Literature data are shown in grey (Steele et al., 2012, 2011; Tang and Dauphas, 2014, 2012). The Ni isotopic data reveal that, for normalization to $^{61}$Ni/$^{58}$Ni, NC meteorites are characterized by deficits in $\mu^{60}$Ni, $\mu^{62}$Ni and $\mu^{64}$Ni, whereas CC meteorites have coupled $\mu^{62}$Ni and $\mu^{64}$Ni excesses and larger $\mu^{60}$Ni deficits. As in previous studies, the $\mu^{62}$Ni and $\mu^{64}$Ni are correlated with a slope of 2.76 ± 0.20 (2$\sigma$). (For interpretation of the colors in the figure(s), the reader is referred to the web version of this article.)

## 3. Results

The Ni isotopic data are reported in Table 1 and plotted in Fig. 1. Data obtained for NIST SRM 986, steel reference material NIST SRM 361, and BHVO-2 (not shown in Fig. 1), are all within analytical uncertainty of zero (Table 1), attesting to the accuracy of the analytical protocol. Furthermore, the results for the IVA iron meteorite Gibeon and CV3 chondrite Allende are in good agreement with those reported previously for these two samples (Steele et al., 2012; Tang and Dauphas, 2014, 2012).

There are resolved Ni isotope variations among the iron meteorites analyzed, but samples from a given chemical group of irons have indistinguishable Ni isotope compositions. For normalization to $^{61}$Ni/$^{58}$Ni, all samples exhibit small $\mu^{60}$Ni deficits and either have coupled $\mu^{62}$Ni and $\mu^{64}$Ni deficits or excesses (Fig. 1). The IC and IIIE irons have Ni isotope anomalies similar to those reported previously for IIAB, IIIAB and IVA irons as well as enstatite and ordinary chondrites (Regelous et al., 2008; Steele et al., 2012, 2011; Tang and Dauphas, 2014, 2012). By contrast, the Ni isotope anomalies of the IIC, IID, IIF, and IIIF irons are similar to those previously reported for IVB irons and carbonaceous chondrites (Fig. 1). As in previous studies (Steele et al., 2012; Tang and Dauphas, 2014, 2012), the $\mu^{62}$Ni and $\mu^{64}$Ni anomalies are strongly correlated and plot on a single line with a slope of ~3 (Fig. 1b).

## 4. Discussion

### 4.1. Ni isotope dichotomy between non-carbonaceous and carbonaceous meteorites

Several prior studies have shown that Ni isotope anomalies in iron meteorites are predominantly nucleosynthetic in origin and can be used to establish genetic links among planetary objects (Regelous et al., 2008; Steele et al., 2011; Tang and Dauphas, 2012). Nevertheless, before utilizing the Ni isotopic data from this study in this manner, it is useful to assess the magnitude of potential radiogenic $^{60}$Ni variations, as well as effects resulting from the interaction with galactic cosmic rays (GCR). Given the limited range of Fe/Ni ratios in bulk iron meteorites (from ~5 to ~15), and the low solar system initial $^{60}$Fe/$^{58}$Fe ratio of ~1 × $10^{-8}$ (Tang and Dauphas, 2014, 2012), potential radiogenic $\mu^{60}$Ni variations among bulk iron meteorites are <0.3 ppm and, hence, insignificant. Cosmic ray-induced isotope variations in iron meteorites are well documented for several elements (e.g., Pt, W) (Kruijer et al., 2013; Qin et al., 2015; Wittig et al., 2013), but for Ni are generally small. They have so far only been identified for one of the most strongly irradiated meteorites, the IVB iron Tlacotopec (Steele et al., 2011). This sample has lower $\mu^{60}$Ni, $\mu^{62}$Ni, and $\mu^{64}$Ni values compared to other, less strongly irradiated IVB irons. However, all irons analyzed in the present study have much smaller GCR-effects than

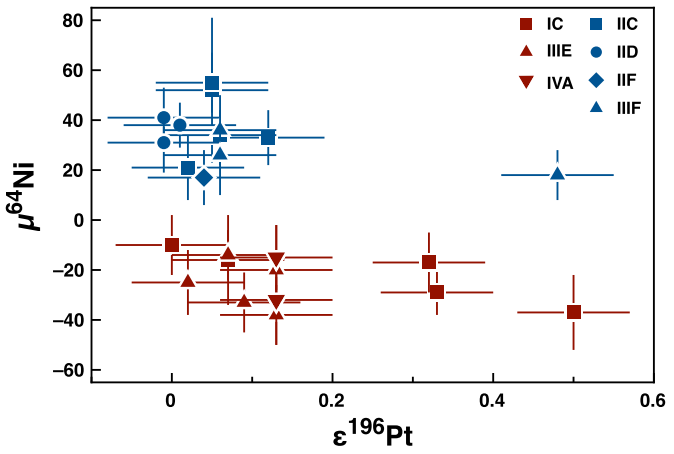


**Fig. 2.** $\mu^{64}$Ni versus $\varepsilon^{196}$Pt for iron meteorites analysed in this study. Positive anomalies in $\varepsilon^{196}$Pt are indicative of GCR-induced neutron capture effects. There is no correlation between Ni isotopic compositions and $\varepsilon^{196}$Pt, demonstrating that GCR-effects are minor to absent. Three IC irons (Murnpeowie, Arispe, Bendego) and the IIIF iron Oakley have $\varepsilon^{196}\text{Pt} > 0.3$ and tend to have slightly lower $\mu^{64}$Ni compared to other samples from the same groups and with smaller $\varepsilon^{196}$Pt. However, for no group are these variations resolved, demonstrating that within the analytical uncertainty of the Ni isotope measurements there are no resolved GCR-effects.

Tlacotepec, as is evident from their smaller Pt isotope anomalies (Table 1). Also, samples from this study with larger GCR-effects (e.g., Bendego, Oakley) do not display resolvable Ni isotope deviations from other, less strongly affected samples of the same group (Fig. 2). Thus, within the analytical uncertainty of the Ni isotope measurements, there are no resolvable GCR-effects in the samples of this study. The observed Ni isotope variations, therefore, are solely nucleosynthetic in origin.

Samples from a given group of magmatic iron meteorites most likely formed by fractional crystallization of isotopically homogeneous metallic magmas. As such, there should be no nucleosynthetic isotope heterogeneity *within* a given chemical group. This is consistent with the Ni isotopic data from this and previous studies, which reveal no resolvable isotope variations among samples from a given chemical group. This observation, together with the absence of significant cosmogenic and radiogenic effects, allows the data for each group to be averaged. Fig. 3 shows the mean Ni isotopic composition for the different groups of iron meteorites, calculated using the Ni isotopic data from this study combined with data from previous studies (see supplement for a summary of all data). Both in $\mu^{60}$Ni–$\mu^{62}$Ni and $\mu^{64}$Ni–$\mu^{62}$Ni space, the iron groups fall into two compositionally distinct clusters. One cluster is characterized by $\mu^{60}$Ni, $\mu^{62}$Ni and $\mu^{64}$Ni deficits and is comprised of several iron groups (IC, IIAB, IIIAB, IIIE, IVA) as well as ordinary and enstatite chondrites. The other cluster is characterized by

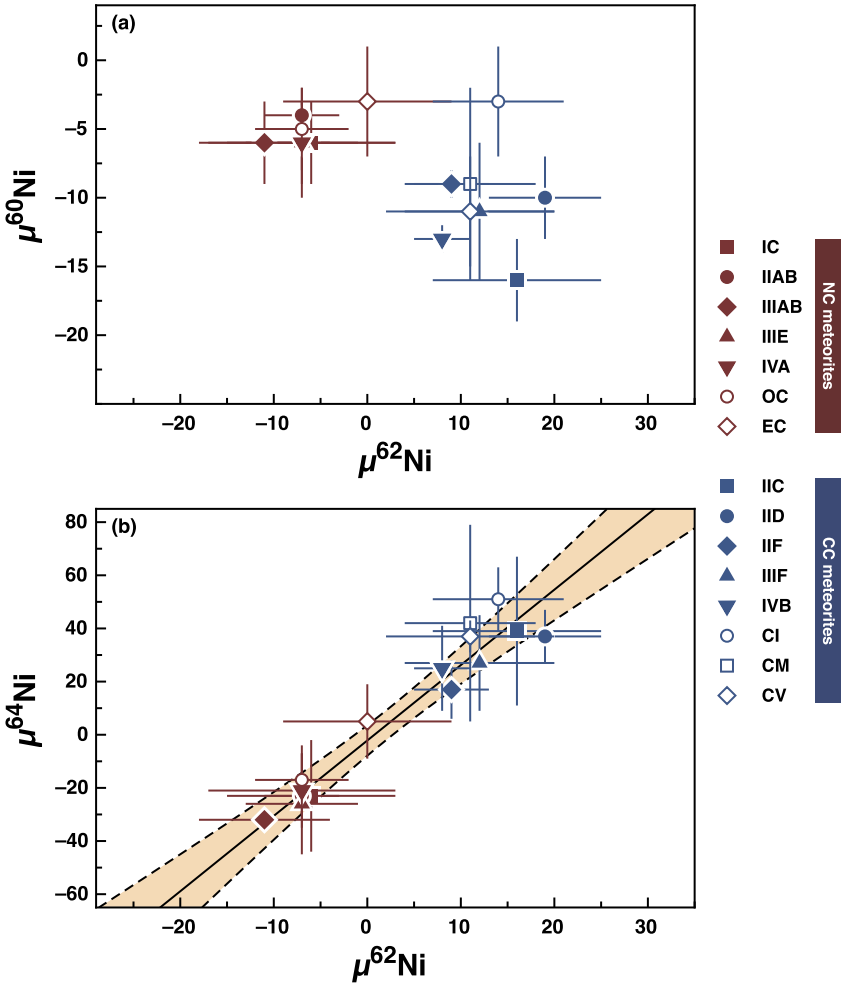


**Fig. 3.** Nickel isotope compositions normalized to $^{61}$Ni/$^{58}$Ni. Except for CI chondrites, group means are shown (see Table S1). The data define two distinct clusters, where the same iron meteorite groups that based on their Mo isotopic signatures are genetically linked to carbonaceous chondrites (IIC, IID, IIF, IIIF, IVB) define one cluster, whereas iron meteorites with non-carbonaceous Mo isotope signatures (IC, IIAB, IIIAB, IIIE, IVA) define the other cluster. As in prior studies, in the $\mu^{62}$Ni versus $\mu^{64}$Ni plot the anomalies plot along a line with a slope of $2.84 \pm 0.57$ ($2\sigma$), consistent with the Ni anomalies mainly residing on $^{58}$Ni.

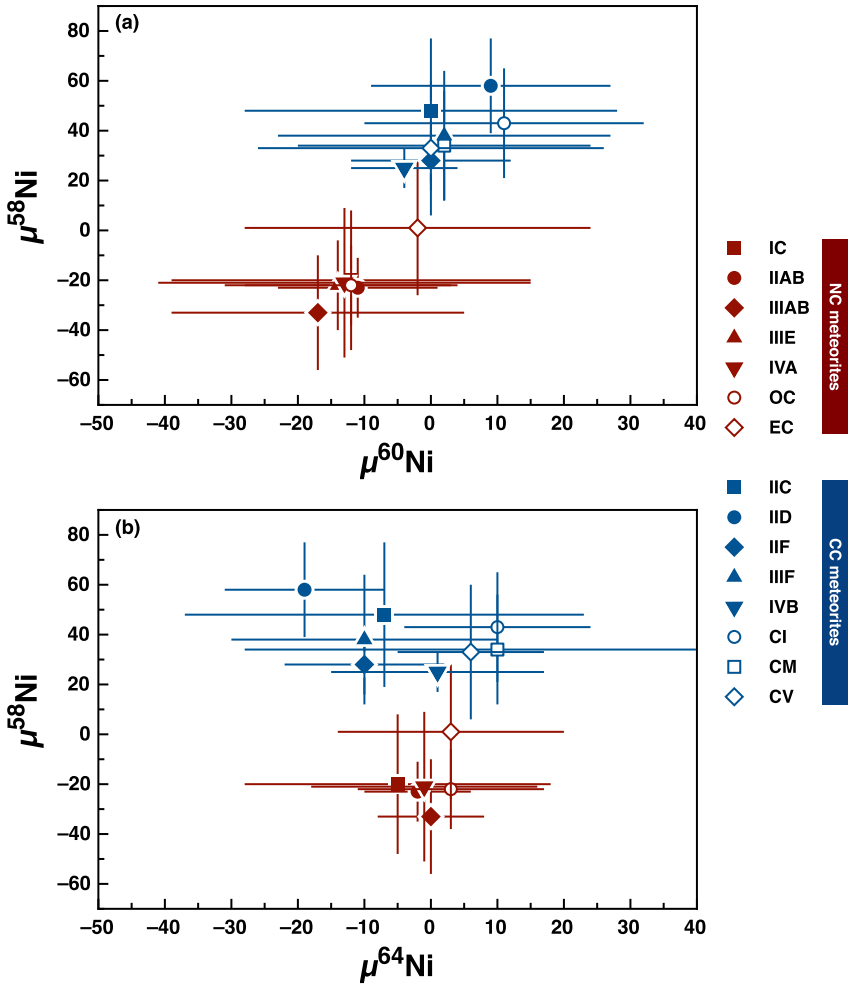


**Fig. 4.** Nickel isotope compositions normalized to $^{62}$Ni/$^{61}$Ni. Except for CI chondrites, group means are shown (see Table S1). CC meteorites are characterized by a fairly uniform $^{58}$Ni excess over NC meteorites, whereas no $^{60}$Ni or $^{64}$Ni differences are resolvable between the NC and CC groups.

slightly larger $\mu^{60}$Ni deficits, but $\mu^{62}$Ni and $\mu^{64}$Ni excesses. This cluster also contains several iron groups (IIC, IID, IIF, IIIF, IVB) as well as carbonaceous chondrites (Fig. 3).

A key observation from the Ni isotopic data is that they reveal the same fundamental dichotomy as observed for Mo isotopes. That is, the same iron meteorite groups that based on their Mo isotopic signatures are genetically linked to carbonaceous chondrites (IIC, IID, IIF, IIIF, IVB), also define the carbonaceous group in Ni isotope space (Fig. 3). Likewise, the same iron meteorites with non-carbonaceous Mo isotope signatures (IC, IIAB, IIIAB, IIIE, IVA) define the non-carbonaceous group in Ni isotope space. Thus, the Ni isotopic data confirm the dichotomy between non-carbonaceous and carbonaceous meteorites defined on the basis of Mo isotopes (Budde et al., 2016; Kruijer et al., 2017), and originally identified using Cr and Ti isotope anomalies in chondrites and differentiated achondrites (Warren, 2011).

### 4.2. Excess $^{58}$Ni in carbonaceous meteorites

Understanding the origin of the Ni isotope dichotomy between non-carbonaceous and carbonaceous meteorites requires identifying the Ni isotope(s) on which the anomalies reside. Earlier work on Ni isotope anomalies reported excesses in $^{62}$Ni and $^{64}$Ni and on this basis inferred that the anomalies are in the neutron-rich isotopes of Ni (Birck and Lugmair, 1988; Quitté et al., 2007). While this is, at least in part, true for Ca, Al-rich inclusions (Render et al., 2018), the anomalies in bulk meteorites seem to have a different origin. Steele et al. (2012) argued that the approximate 3:1 relationship between $\mu^{62}$Ni and $\mu^{64}$Ni observed for bulk meteorites is consistent with an anomaly on $^{58}$Ni alone. These authors also reported absolute Ni isotope ratios for two chondrites (obtained by the double spike method), which support the conclusion that the Ni isotope anomalies predominantly reside on $^{58}$Ni.

As in previous studies, the Ni isotopic data of the present study also reveal a $\mu^{62}$Ni–$\mu^{64}$Ni correlation with a slope of ~3 (Fig. 1b, 3b), consistent with variable anomalies on $^{58}$Ni. Moreover, when internally normalized to a fixed $^{62}$Ni/$^{61}$Ni (Table 1; Fig. 4), there is a consistent offset in $\mu^{58}$Ni between carbonaceous and non-carbonaceous meteorites (Fig. 4). By contrast, there are no resolved anomalies in $\mu^{60}$Ni and $\mu^{64}$Ni between these two groups of meteorites, although the carbonaceous meteorites tend to have higher $\mu^{60}$Ni compared to the non-carbonaceous meteorites (Fig. 4). Overall, these data are, therefore, consistent with anomalies predominantly residing on $^{58}$Ni. Note that the uncertainties on the Ni isotopic data are too large to resolve potential $^{58}$Ni variations among the different members of the NC and CC groups. Nevertheless, the $\mu^{58}$Ni difference *between* the NC and CC groups is well resolved, and the difference between the mean $\mu^{58}$Ni values of both groups is ~60 ppm (Fig. 4). Thus, the CC reservoir is characterized by a fairly homogeneous $^{58}$Ni excess over the NC reservoir.

Prior work has shown that the CC reservoir is characterized by excesses in $^{54}$Cr and $^{50}$Ti (Trinquier et al., 2007; Trinquier et al., 2009; Warren, 2011), and *r*-process Mo isotopes (Budde et al., 2016). These nuclides have in common that they are produced in

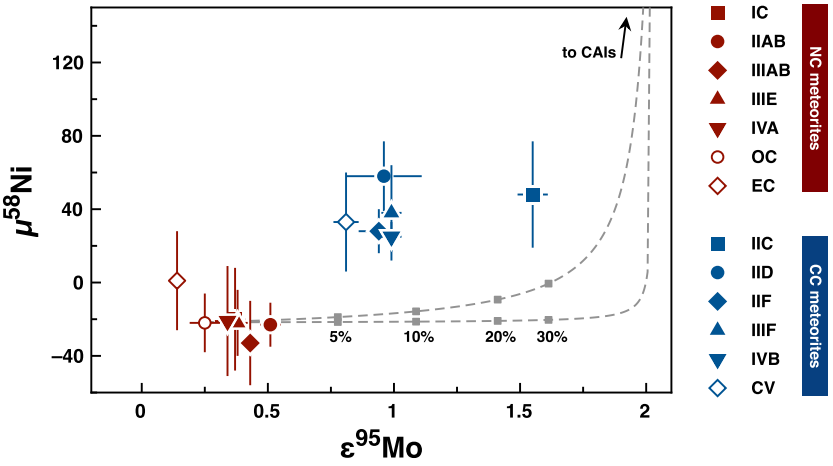


**Fig. 5.** $\mu^{58}$Ni versus $\varepsilon^{95}$Mo for iron meteorites and chondrites. Mo isotopic data are from the literature (Budde et al., 2016; Kruijer et al., 2017; Render et al., 2017). Of the carbonaceous chondrites, only CV chondrites are shown, because only for those have Mo and Ni isotopic data been obtained on the same sample (i.e., Allende MS-A; Budde et al., 2016 and this study). Grey dashed line is a mixing line between an average NC composition ($\mu^{58}$Ni = −22; $\varepsilon^{95}$Mo = 0.25) and CAIs; for the CAIs $\mu^{58}$Ni = 413 and $\varepsilon^{95}$Mo = 2 were assumed (Render et al., 2018). The $\mu^{58}$Ni is the largest anomaly reported for CAIs, whereas $\varepsilon^{95}$Mo = 2 is the average value for coarse-grained CAI (Brennecka et al., 2013; Burkhardt et al., 2011). The upper mixing line assumes 120 ppm Ni in CAI, whereas the lower line assumes 2000 ppm Ni; these two concentrations cover the range of Ni concentrations reported for CAIs (Birck and Lugmair, 1988). The other assumed concentrations are 8 ppm Mo in CAIs, and 1 ppm Mo and 16 wt-% Ni in bulk chondrites (Burkhardt et al., 2011; Wasson and Kallemeyn, 1988).

neutron-rich stellar environments, such as supernovae. This is consistent with the $^{58}$Ni excess of the CC reservoir observed in the present study, because, although $^{58}$Ni is a neutron-poor Ni isotope itself, it is produced during supernova nuclear burning. The general characteristic of the CC compared to the NC reservoir, therefore, is a relative enrichment of nuclides produced in neutron-rich stellar environments.

### 4.3. Origin of the NC–CC dichotomy by infall

The isotopic difference between the NC and CC reservoirs could in principle result from processes within the disk itself, such as transport of isotopically anomalous components or thermal processing of presolar carriers, which may have been different in different areas of the disk. Alternatively, the NC–CC dichotomy may be an inherited isotopic heterogeneity from the solar system's parental molecular cloud core. The Ni isotopic data of the present study, together with isotopic data from previous studies, can be used to explore these different possibilities.

Many of the isotopic characteristics of the CC reservoir, such as the enrichment in $^{54}$Cr, $^{50}$Ti, and *r*-process Mo, can also be found in CAIs. Thus, addition of CAIs to the CC reservoir could in principle account for the distinct Mo isotope compositions of the NC and CC reservoirs. Assuming that CAIs formed close to the Sun, such a model would require disk wide transport of CAI to the CC region, which presumably was located beyond the orbit of Jupiter. However, the Ni isotope dichotomy observed in the present study cannot be explained in this manner, because CAIs contain too little Ni to have a significant effect on the Ni isotopic composition of the CC reservoir. By contrast to Mo, which is a refractory element ($T_{50\%}$ = 1590 K) and strongly enriched in CAIs (∼10 × CI), Ni is not refractory ($T_{50\%}$ = 1353 K) and condenses together with the main mass of the condensable matter (the 'main component') (Lodders, 2003). As such, Ni is depleted in CAIs compared to bulk chondrites, meaning that addition of CAI-material has a negligible effect on the Ni isotopic composition of bulk meteorites and is not the cause for excess $^{58}$Ni in CC materials. This is illustrated in a plot of $^{58}$Ni versus $^{95}$Mo, where the CC and NC meteorites form two distinct clusters, showing that the CC reservoir is characterized by excesses in $^{95}$Mo and $^{58}$Ni over the NC reservoir (Fig. 5). The very different Mo/Ni ratios in CAIs and bulk chondrites result in strongly curved mixing lines in this diagram, illustrating that whereas the $^{95}$Mo excess of the CC reservoir could be reproduced by the addition of ∼5–10% CAI-like material, the $^{58}$Ni composition of this mixture remains unchanged (Fig. 5). Thus, the Ni isotopic data rule out that the distinct isotopic compositions of the NC and CC reservoirs solely reflect an overabundance of CAI-like material in the latter.

The compositional difference between the NC and CC reservoirs is also unlikely to reflect removal of isotopically anomalous material from the NC reservoir, for instance through thermal processing. This would require the very efficient removal of presolar components that were likely hosted in different carriers over a wide range of volatility (Mo, Ni, Cr, Ti). It would also require that carriers formed in neutron-rich stellar environments were preferentially affected, while the effects of thermal processing depend on the thermal stability of a given presolar carrier, and not on the stellar environment in which this carrier formed.

Thus, the most straightforward interpretation is that the NC–CC dichotomy reflects the addition of isotopically distinct material whose bulk *chemical* composition was broadly similar to average solar system matter, because such material would have affected refractory and non-refractory elements in a similar manner. Either bulk material containing a larger fraction of presolar carriers enriched in nuclides produced in neutron-rich environments (i.e., *r*-process Mo, $^{58}$Ni, $^{50}$Ti, $^{54}$Cr) was added primarily to a region that became the CC reservoir or, alternatively, bulk material depleted in these carriers was added primarily to the region that became the NC reservoir. In both cases, no selective processing of several specific carriers is necessary, because the isotopic difference between the NC and CC reservoirs solely reflects a temporal or spatial change in the composition of the material that is accreted to the disk during infall from the collapsing protostellar envelope. The isotopic composition of the infalling material may have changed over time because this material derives from different parts of a compositionally heterogeneous parental molecular cloud, or because the composition of the cloud itself changed over time. Either way, formation of the NC–CC dichotomy during infall implies that the nucleosynthetic isotope difference between the NC and CC reservoirs is inherited from the solar system's parental molecular cloud.

### 4.4. Effects of infall on the isotopic composition of the disk

To assess how a change in the isotopic composition of the infalling material would affect the composition of the disk, we considered two simple early nebula models with ongoing infall, based on Hueso and Guillot (2005). This model shows that disks grow larger even without allowing for viscous expansion as the angular momentum of the infalling material increases over time. Our simple models neglect viscous spreading (e.g., Yang and Ciesla, 2012) and diffusive radial mixing (Visser et al., 2009), so should be regarded only as a crude indication of how infall might affect the local composition of the disk.

Two cases were considered, which primarily differ in the assumption of whether or not rapid viscous radial expansion of early-infalling material occurred. This rapid expansion is expected due to viscosity or gravitational instability (e.g., Cassen and Moosman, 1981; Hueso and Guillot, 2005; Yang and Ciesla, 2012), and would have essentially formed a pre-existing disk onto which material later falls. In the first case considered, no pre-existing disk is assumed and material remains where it falls; this is the inviscid endmember of models by Hueso and Guillot (2005). A change in the composition of infalling material would naturally result in a larger effect in the outer disk than the inner disk precisely because there is no prior material there to mix with. The disk gets larger only by accumulating newly infalling material with higher angular momentum, so that more distant regions of the disk are more sensitive to the later composition of infalling material. Fig. 6a demonstrates this effect, where the solid lines show the disk surface density at four different times, and illustrate the radial growth of the disk directly from infalling material. The crosses show the fraction of material delivered to a particular location after 0.22 Ma. In the outer disk, all material is delivered after this time, but in the inner disk, most of the material is delivered earlier. As a result, a change in composition of the infalling material at 0.22 Ma would have a much larger effect on the outer disk (Fig. 6a). The radius at which the strongest radial variation occurs is where material is currently infalling, which is the so-called centrifugal radius (Hueso and Guillot, 2005) and depends on the uncertain angular momentum per unit mass of the parent cloud. Note that the time of 0.22 Ma, as well as the individual time steps, are arbitrary and only serve to illustrate the effect of late infall on the composition of the outer disk. The NC–CC dichotomy in this case requires the later infalling material to have a CC-like composition, because the composition of the outer disk (i.e., the CC reservoir) is determined by the late infall.

The second case uses the same infall model, but now assumes an initial disk is present, with a radial distribution proportional to $r^{-1/2}$. This initial disk represents about 4% of the total final mass of the disk, and is merely a convenient proxy for material emplaced there due to rapid viscous radial expansion at earlier times. The crosses now show the mass fraction delivered after the start of infall (Fig. 6b), demonstrating that in the inner disk all the mass comes in with the infall, but in the outermost disk all the material is from the earlier rapid spreading. The NC–CC dichotomy in this case requires later infall to be relatively *depleted* in nuclides produced in neutron-rich stellar environments (i.e., those nuclides that are *enriched* in the CC reservoir). The results shown in Fig. 6b are supported by more sophisticated models by Yang and Ciesla (2012; their Fig. 7). These authors have shown that the abundance of early, high-temperature material inside of the centrifugal radius is diluted by addition of new material that has never been strongly heated. These authors also showed that the abundance of high-temperature material is greater again at larger heliocentric distance, outside of the centrifugal radius. This result is consistent with ours, shown in Fig. 6b, indicating that the outermost disk retains its composition (resulting from early viscous spreading), whereas the composition of the inner disk is modified by later infall.

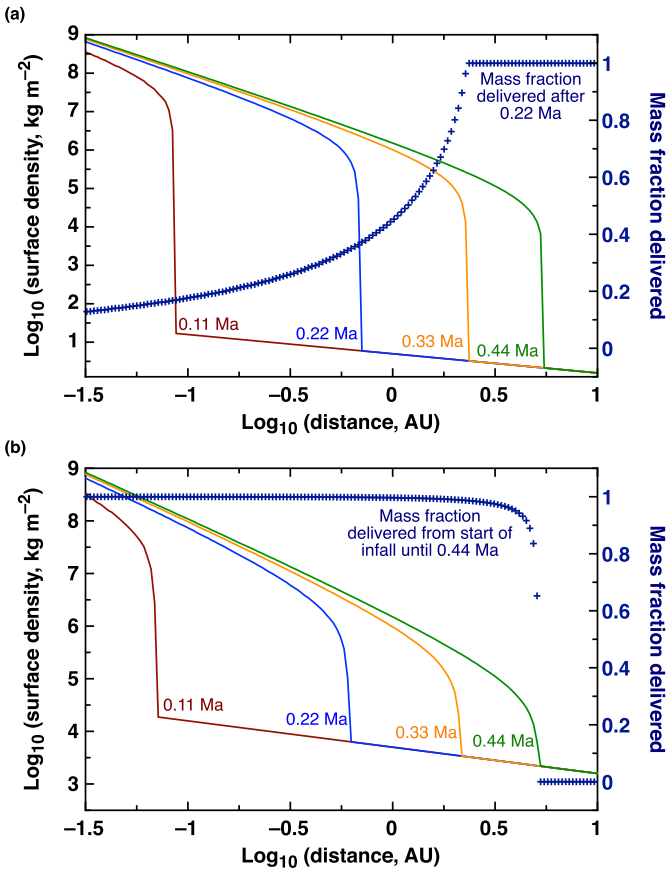


**Fig. 6.** Growth of disk surface density with time, using the expressions for infall rate in Hueso and Guillot (2005) and neglecting disk viscous evolution. In this example we took the disk temperature to be 10 K and the cloud angular frequency to be $5 \times 10^{-15}$ rad s$^{-1}$, but the qualitative result is not affected by these parameter choices. The constant mass accretion rate is 1.68 solar masses/Ma. **(a)** No initial disk was present. The crosses denote the fraction of mass delivered after 0.22 Ma to a particular distance. **(b)** An initial disk was present with a flatter surface density distribution as in (a), representing about 4% of the total final mass. The crosses denote the mass fraction delivered after the start of the infall. In the inner disk essentially all the mass comes in with the infall, whereas in the outermost disk the material is still from the original, pre-existing disk.

Although the results of Fig. 6 are based on very simplified calculations, they nevertheless show at least qualitatively that a compositional change of the infalling material affects different areas of the disk differently, potentially resulting in the formation of the isotopically distinct NC and CC reservoirs. The calculations also show that the outcome is very sensitive to the assumption of whether or not a pre-existing disk (resulting from rapid earlier expansion) was present. Although more sophisticated disk models than those used here exist, 1D models likely oversimplify the complicated processes of disk formation and evolution (Visser et al., 2009). As such, there is little hope that models as simple as those shown in Fig. 6 alone will be able to distinguish between the two cases considered above. However, as will be shown below, the distinct isotopic compositions of components in NC and CC chondrites, and especially the isotopic composition of CAIs, provide important clues.

### 4.5. Evidence from the genetic link between CAIs and the CC reservoir

As noted above, many of the isotopic characteristics of the CC reservoir can also be found in CAIs, which are known to have formed very early (Connelly et al., 2012; MacPherson et al., 2012).

Thus, there is an obvious genetic link between CAIs—the oldest dated solids of the solar system which are commonly thought to have formed close to the Sun—and the CC reservoir, which presumably was located in the outer solar system and contains some of the latest-formed meteorite parent bodies. These seemingly contradictory observations hold important clues as to how the NC–CC dichotomy ultimately formed.

The two models considered above for the formation of the NC–CC dichotomy by infall make very different predictions about the formation location of CAIs. The first case, where the CC reservoir formed from late-infalling material, necessitates that CAIs formed in the outer solar system because this is where material with the isotopic characteristic of CAI is infalling in this model. Moreover, in this particular model, there is no viscous spreading of the disk, and so there is no mechanism for transporting CAIs from near the Sun to the CC region where they were incorporated into carbonaceous chondrite parent bodies. However, formation of CAIs requires high temperatures (>1300 K; Grossman, 1972), which are commonly thought to have persisted only close to the Sun (<1 AU; Yang and Ciesla, 2012). As to whether such high temperatures existed elsewhere in the disk is unknown, but regardless the most obvious high-temperature environment in the early solar system is close to the Sun. Moreover, in this model CAIs would have formed from late-infalling material and, therefore, after the inner disk (i.e., the NC reservoir) had already formed. As such, there should be material in the NC reservoir which is older than CAIs, however, there is no evidence in the meteorite record that such material existed. It is possible that such earlier material has been completely reprocessed and included into later formed objects, but this interpretation is quite ad hoc. Given these problems, combined with the requirement that early viscous expansion of the disk was completely lacking, the scenario in which the CC reservoir represents the late-infalling material seems less plausible.

In the second case, where an initial disk formed by rapid radial expansion of early-infalling material, CAIs would have formed close to the Sun and were subsequently transported outwards, presumably by the same process that produced the underlying disk upon which NC-like material later falls. The strength of this model is that it naturally accounts (*i*) for the formation of CAIs close to the Sun, (*ii*) for their outward transport, and (*iii*) for the isotopic link between CAIs and the CC reservoir, by essentially the same process, namely the rapid radial expansion of early-infalling material.

It is noteworthy that CAIs are extremely rare in the NC reservoir, which might imply that the outward transport process was very efficient. Alternatively, as most of the mass of the inner disk would derive from the later infall of NC material, any pre-existing CAIs in the inner disk may have simply been strongly diluted. These two processes are not mutually exclusive and provide viable mechanisms for why NC chondrites are virtually devoid of CAIs. Consistent with this, the few CAIs that exist in NC chondrites are isotopically indistinguishable from CAIs in carbonaceous chondrites, indicating derivation from a common source reservoir and hence formation location in the disk (Ebert et al., 2018; McKeegan et al., 1998; Russell et al., 1996). Of note, some NC chondrules—i.e., Na-Al-rich chondrules from ordinary chondrites—show evidence for the incorporation of CAI-like refractory material into their precursors. Surprisingly though, these chondrules do not show the typical $^{50}$Ti excesses observed for CAIs, implying that there has been refractory material within the NC reservoir that is distinct from known CAIs (Ebert et al., 2018). One possibility is that this refractory component formed slightly later than known CAIs, at a time when the inner disk already had a NC composition. For instance, Yang and Ciesla (2012) have shown that formation of refractory components may have occurred over several hundred thousand years out to 1 AU (their Fig. 3); thus, if during this process the isotopic composition of the inner disk changed from CAI-like to NC, then later-formed refractory components may have had a NC composition.

Fig. 7 is a cartoon illustrating our preferred scenario for the compositional evolution of the disk during infall and the formation of the NC–CC dichotomy. In this model, CAIs formed close to the Sun during the earliest stage of infall, and were transported outwards by rapid radial expansion of the early infalling material. Later infalling material, which provides most of the mass of the inner disk, was isotopically distinct and, compared to the earlier infalling material, depleted in supernova-derived nuclides of elements like Cr, Ti, Ni, and Mo. As most of the material in the inner disk derives from this infall, this later infalling material likely had a NC-like composition. In the outer disk, beyond the radius at which material is infalling, the composition of the initial disk is preserved, but likely became diluted through mixing between inner and outer disk material. The final isotopic composition of the CC reservoir can therefore be regarded as being intermediate between the initial isotopic composition of the earliest disk and the composition of the inner disk as given by the NC reservoir. Although the initial isotopic composition of the disk is unknown, it probably was similar to that measured for CAIs, most of which display stronger enrichments in $^{50}$Ti, $^{54}$Cr, and *r*-process Mo than the CC reservoir. Note that although CAIs may represent the *isotopic* composition of the earliest disk, their *chemical* composition is drastically different.

After the infall of material ceased, the proto-Sun continued to accrete material from its disk, as a result of inward transport of mass and outward movement of angular momentum (Hueso and Guillot, 2005; Yang and Ciesla, 2012). Thus, to avoid complete homogenization and to maintain an isotopic difference between the CC and NC reservoirs, the inward transport of outer disk material must have been at least partially blocked before planetesimal formation in the CC reservoir had begun (i.e., prior to ∼1 Ma after CAI formation). This most likely occurred when Jupiter's core grew large enough to prohibit significant material exchange between material inside (the NC reservoir) and outside (the CC reservoir) its orbit (Kruijer et al., 2017). Further work is needed to assess how nebula gas can be allowed to drain into the Sun over a fraction of a Ma, even while solids remain isolated in their separate regions.

### 4.6. Origin of the isotopic change of infalling material

It seems tempting to link the early infall of material enriched in supernova-derived nuclides to the proposed supernova-trigger for the formation of the solar system (Cameron and Truran, 1977). In such a model, the early-infalling material would derive from the supernova trigger, whereas the later-infalling material would derive from the molecular cloud itself. It is important to recognize, however, that the enrichment in supernova-derived nuclides for elements like Cr, Ti, Ni and Mo does not provide any constraint on the relative timing of the supernova and the formation of the solar system. Unlike for short-lived radionuclides (e.g., $^{26}$Al, $^{60}$Fe), the abundances of these nuclides do not decrease after their production, and so the supernova-enriched material may have been injected into the molecular cloud at any time prior to collapse and solar system formation. As such, the isotopic variation of the infalling material cannot be linked to a specific event around the time of solar system formation, but instead reflects an isotopic heterogeneity within the solar system's parental molecular cloud, which has been maintained within the solar accretion disk because material infalling at different times derives from different parts of the parent cloud.

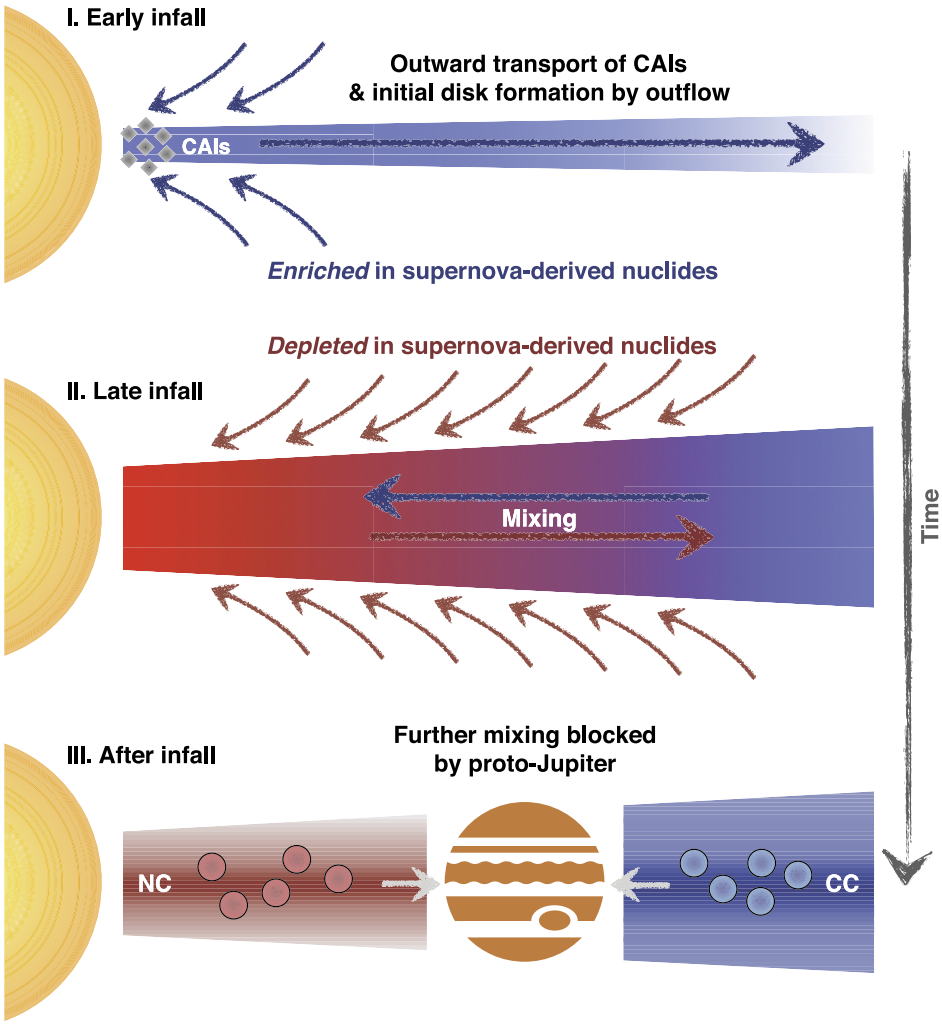


**Fig. 7.** Cartoon illustrating the formation of the NC–CC dichotomy by late infall of isotopically distinct material (not to scale). Rapid expansion of early infalling material by viscous spreading produces an initial disk, whose isotopic composition may be recorded in CAIs. Later infalling material dominates the composition of the inner disk and in this case has a NC composition, i.e., it is depleted in supernova-derived nuclides such as $^{50}$Ti, $^{54}$Cr, $^{58}$Ni, *r*-process Mo. Mixing within the disk likely reduced the initial isotopic difference between solids from the inner and outer disk, but the rapid formation of Jupiter's core prevented complete homogenization, maintaining an isotopic difference between the NC and CC reservoirs.

## 5. Conclusions

Carbonaceous meteorites exhibit a fairly uniform $^{58}$Ni excess over non-carbonaceous meteorites. Combined with prior observations for other elements, this indicates that the CC reservoir contains a larger fraction of presolar carriers enriched in nuclides produced in neutron-rich stellar environments (i.e., *r*-process Mo, $^{58}$Ni, $^{50}$Ti, $^{54}$Cr), and that the NC–CC dichotomy exists for both refractory (Ti, Mo) and non-refractory (Ni, Cr) elements. These observations are best accounted for if the NC–CC dichotomy reflects a compositional change of the infalling material from the solar system's protostellar envelope.

Many of the isotopic characteristics of the CC reservoir can also be found in CAIs, but with smaller enrichments. This observation, combined with evidence that CAIs formed close to the young Sun, suggests that CAIs are representative of the isotopic composition of the earliest disk, which formed by rapid viscous expansion during early infall. The composition of the inner disk would then be dominated by the later infall of material depleted in supernova-derived nuclides, resulting in the formation of the NC reservoir. By contrast, some signature of the earliest disk is preserved, in diluted form, as the composition of the CC reservoir. Once the infall ceased, diffusive mixing and radial drift of solids would have homogenized the isotopic difference between the NC and CC reservoirs. This homogenization was likely prevented by the rapid formation of Jupiter's core, which maintained an isotopic difference between solid material inside (NC reservoir) and outside (CC reservoir) its orbit. The NC–CC dichotomy, therefore, reflects an inherited isotopic heterogeneity from the solar system's parental molecular cloud, which was established during infall from the Sun's protostellar envelope and has been preserved through the rapid formation of Jupiter.

## Acknowledgements

We gratefully acknowledge the Natural History Museum, London, the Field Museum of Natural History, Chicago, and the Smithsonian Institution National Museum of Natural History, Washington D.C., for providing samples for this study. We are grateful to G. Brennecka, G. Budde, C. Burkhardt, T.S. Kruijer, J. Render, and E. Worsham for fruitful discussion and comments, to Haolan Tang and an anonymous referee for constructive reviews, and to Fred Moynier for efficient editorial handling. The work was supported by the European Research Council Consolidator Grant 'ISOCORE' to T.K. (contract no. 616564), which is gratefully acknowledged.

## Appendix A. Supplementary material

Supplementary material related to this article can be found online at https://doi.org/10.1016/j.epsl.2019.01.027.

## References


Birck, J.L., Lugmair, G.W., 1988. Nickel and chromium isotopes in Allende inclusions. Earth Planet. Sci. Lett. 90, 131–143.

Brennecka, G.A., Borg, L.E., Wadhwa, M., 2013. Evidence for supernova injection into the solar nebula and the decoupling of *r*-process nucleosynthesis. Proc. Natl. Acad. Sci. USA 110, 17241–17246.

Budde, G., Burkhardt, C., Brennecka, G.A., Fischer-Gödde, M., Kruijer, T.S., Kleine, T., 2016. Molybdenum isotopic evidence for the origin of chondrules and a distinct genetic heritage of carbonaceous and non-carbonaceous meteorites. Earth Planet. Sci. Lett. 454, 293–303.

Budde, G., Kruijer, T.S., Kleine, T., 2018. Hf–W chronology of CR chondrites: implications for the timescales of chondrule formation and the distribution of $^{26}$Al in the solar nebula. Geochim. Cosmochim. Acta 222, 284–304.

Burbidge, E.M., Burbidge, G.R., Fowler, W.A., Hoyle, F., 1957. Synthesis of the elements in stars. Rev. Mod. Phys. 29, 547–650.

Burkhardt, C., Kleine, T., Dauphas, N., Wieler, R., 2012. Origin of isotopic heterogeneity in the solar nebula by thermal processing and mixing of nebular dust. Earth Planet. Sci. Lett. 357–358, 298–307.

Burkhardt, C., Kleine, T., Oberli, F., Pack, A., Bourdon, B., Wieler, R., 2011. Molybdenum isotope anomalies in meteorites: constraints on solar nebula evolution and origin of the Earth. Earth Planet. Sci. Lett. 312, 390–400.

Cameron, A.G.W., Truran, J.W., 1977. The supernova trigger for formation of the Solar System. Icarus 30, 447–461.

Cassen, P., Moosman, A., 1981. On the formation of protostellar disks. Icarus 48, 353–376.

Chernonozhkin, S.M., Goderis, S., Lobo, L., Claeys, P., Vanhaecke, F., 2015. Development of an isolation procedure and MC–ICP–MS measurement protocol for the study of stable isotope ratio variations of nickel. J. Anal. At. Spectrom. 30, 1518–1530.

Connelly, J.N., Bizzarro, M., Krot, A.N., Nordlund, A., Wielandt, D., Ivanova, M.A., 2012. The absolute chronology and thermal processing of solids in the solar protoplanetary disk. Science 338, 651–655.

Dauphas, N., Schauble, E.A., 2016. Mass fractionation laws, mass-independent effects, and isotopic anomalies. Annu. Rev. Earth Planet. Sci., 709–783.

Ebert, S., Render, J., Brennecka, G.A., Burkhardt, C., Bischoff, A., Gerber, S., Kleine, T., 2018. Ti isotopic evidence for a non-CAI refractory component in the inner Solar System. Earth Planet. Sci. Lett. 498, 257–265.

Gerber, S., Burkhardt, C., Budde, G., Metzler, K., Kleine, T., 2017. Mixing and transport of dust in the early solar nebula as inferred from titanium isotope variations among chondrules. Astrophys. J. Lett. 841, L17.

Gramlich, J.W., Machlan, L.A., Barnes, I.L., Paulsen, P.J., 1989. Absolute isotopic abundance ratios and atomic weight of a reference sample of nickel. J. Res. Natl. Inst. Stand. Technol. 94, 347–356.

Grossman, L., 1972. Condensation in the primitive solar nebula. Geochim. Cosmochim. Acta 36, 597–619.

Hueso, R., Guillot, T., 2005. Evolution of protoplanetary disks: constraints from DM Tauri and GM Aurigae. Astron. Astrophys. 442, 703–725.

Kita, N.T., Ushikubo, T., 2012. Evolution of protoplanetary disk inferred from $^{26}$Al chronology of individual chondrules. Meteorit. Planet. Sci. 47, 1108–1119.

Kleine, T., Budde, G., Hellmann, J.L., Kruijer, T.S., Burkhardt, C., 2018. Tungsten isotopes and the origin of chondrules and chondrites. In: Krot, A.N., Connolly Jr., H.C., Russell, S.S. (Eds.), Chondrules: Records of Protoplanetary Disk Processes. Cambridge University Press, Cambridge, pp. 276–299.

Krot, A.N., Amelin, Y., Bland, P., Ciesla, F.J., Connelly, J., Davis, A.M., Huss, G.R., Hutcheon, I.D., Makide, K., Nagashima, K., Nyquist, L.E., Russell, S.S., Scott, E.R.D., Thrane, K., Yurimoto, H., Yin, Q.Z., 2009. Origin and chronology of chondritic components: a review. Geochim. Cosmochim. Acta 73, 4963–4997.

Kruijer, T.S., Burkhardt, C., Budde, G., Kleine, T., 2017. Age of Jupiter inferred from the distinct genetics and formation times of meteorites. Proc. Natl. Acad. Sci. USA 114, 6712–6716.

Kruijer, T.S., Fischer-Gödde, M., Kleine, T., Sprung, P., Leya, I., Wieler, R., 2013. Neutron capture on Pt isotopes in iron meteorites and the Hf–W chronology of core formation in planetesimals. Earth Planet. Sci. Lett. 361, 162–172.

Kruijer, T.S., Touboul, M., Fischer-Godde, M., Bermingham, K.R., Walker, R.J., Kleine, T., 2014. Protracted core formation and rapid accretion of protoplanets. Science 344, 1150–1154.

Lodders, K., 2003. Solar system abundances and condensation temperatures of the elements. Astrophys. J. 591, 1220–1247.

MacPherson, G.J., Kita, N.T., Ushikubo, T., Bullock, E.S., Davis, A.M., 2012. Well-resolved variations in the formation ages for Ca–Al-rich inclusions in the early Solar system. Earth Planet. Sci. Lett. 331–332, 43–54.

Matthes, M., Fischer-Gödde, M., Kruijer, T.S., Kleine, T., 2018. Pd–Ag chronometry of IVA iron meteorites and the crystallization and cooling of a protoplanetary core. Geochim. Cosmochim. Acta 220, 82–95.

McKeegan, K.D., Leshin, L.A., Russell, S.S., MacPherson, G.J., 1998. Oxygen isotopic abundances in calcium–aluminum-rich inclusions from ordinary chondrites: implications for nebular heterogeneity. Science 280, 414–418.

Nagashima, K., Krot, A.N., Komatsu, M., 2017. $^{26}$Al–$^{26}$Mg systematics in chondrules from Kaba and Yamato 980145 CV3 carbonaceous chondrites. Geochim. Cosmochim. Acta 201, 303–319.

Poole, G.M., Rehkämper, M., Coles, B.J., Goldberg, T., Smith, C.L., 2017. Nucleosynthetic molybdenum isotope anomalies in iron meteorites – new evidence for thermal processing of solar nebula material. Earth Planet. Sci. Lett. 473, 215–226.

Qin, L., Dauphas, N., Horan, M.F., Leya, I., Carlson, R.W., 2015. Correlated cosmogenic W and Os isotopic variations in Carbo and implications for Hf–W chronology. Geochim. Cosmochim. Acta 153, 91–104.

Quitté, G., Halliday, A.N., Meyer, B.S., Markowski, A., Latkoczy, C., Günther, D., 2007. Correlated iron 60, nickel 62, and zirconium 96 in refractory inclusions and the origin of the solar system. Astrophys. J. 655, 678–684.

Regelous, M., Elliott, T., Coath, C.D., 2008. Nickel isotope heterogeneity in the early Solar system. Earth Planet. Sci. Lett. 272, 330–338.

Render, J., Brennecka, G.A., Wang, S.-J., Wasylenki, L.E., Kleine, T., 2018. A distinct nucleosynthetic heritage for early solar system solids recorded by Ni isotope signatures. Astrophys. J. 862, 26.

Render, J., Fischer-Gödde, M., Burkhardt, C., Kleine, T., 2017. The cosmic molybdenum–neodymium isotope correlation and the building material of the Earth. Geochem. Perspect. Lett. 3, 170–178.

Russell, S.S., Srinivasan, G., Huss, G.R., Wasserburg, G.J., Macpherson, G.J., 1996. Evidence for widespread $^{26}$Al in the solar nebula and constraints on nebula time scales. Science 273, 757–762.

Steele, R.C.J., Coath, C.D., Regelous, M., Russell, S., Elliott, T., 2012. Neutron-poor nickel isotope anomalies in meteorites. Astrophys. J. 758.

Steele, R.C.J., Elliott, T., Coath, C.D., Regelous, M., 2011. Confirmation of mass-independent Ni isotopic variability in iron meteorites. Geochim. Cosmochim. Acta 75, 7906–7925.

Tang, H.L., Dauphas, N., 2012. Abundance, distribution, and origin of Fe-60 in the solar protoplanetary disk. Earth Planet. Sci. Lett. 359, 248–263.

Tang, H., Dauphas, N., 2014. $^{60}$Fe–$^{60}$Ni chronology of core formation in Mars. Earth Planet. Sci. Lett. 390, 264–274.

Trinquier, A., Birck, J.L., Allègre, C.J., 2007. Widespread $^{54}$Cr heterogeneity in the inner solar system. Astrophys. J. 655, 1179–1185.

Trinquier, A., Elliott, T., Ulfbeck, D., Coath, C., Krot, A.N., Bizzarro, M., 2009. Origin of nucleosynthetic isotope heterogeneity in the solar protoplanetary disk. Science 324, 374–376.

Ushikubo, T., Nakashima, D., Kimura, M., Tenner, T.J., Kita, N.T., 2013. Contemporaneous formation of chondrules in distinct oxygen isotope reservoirs. Geochim. Cosmochim. Acta 109, 280–295.

Villeneuve, J., Chaussidon, M., Libourel, G., 2009. Homogeneous distribution of $^{26}$Al in the Solar System from the Mg isotopic composition of chondrules. Science 325, 985–988.

Visser, R., van Dishoeck, E.F., Doty, S.D., Dullemond, C.P., 2009. The chemical history of molecules in circumstellar disks. I. Ices. Astron. Astrophys. 495, 881–897.

Warren, P.H., 2011. Stable-isotopic anomalies and the accretionary assemblage of the Earth and Mars: a subordinate role for carbonaceous chondrites. Earth Planet. Sci. Lett. 311, 93–100.

Wasson, J.T., Kallemeyn, G.W., 1988. Compositions of chondrites. Philos. Trans. R. Soc. Lond. 325, 535–544.

Wittig, N., Humayun, M., Brandon, A.D., Huang, S., Leya, I., 2013. Coupled W–Os–Pt isotope systematics in IVB iron meteorites: in situ neutron dosimetry for W isotope chronology. Earth Planet. Sci. Lett. 361, 152–161.

Worsham, E.A., Bermingham, K.R., Walker, R.J., 2017. Characterizing cosmochemical materials with genetic affinities to the Earth: genetic and chronological diversity within the IAB iron meteorite complex. Earth Planet. Sci. Lett. 467, 157–166.

Yang, L., Ciesla, F.J., 2012. The effects of disk building on the distributions of refractory materials in the solar nebula. Meteorit. Planet. Sci. 47, 99–119.